A staggered multiphysics framework for salt crystallization-induced damage in porous building materials

Published Version:
Castellazzi G., D'Altri A.M., de Miranda S., Emami H., Molari L., Ubertini F. (2021). A staggered multiphysics framework for salt crystallization-induced damage in porous building materials. CONSTRUCTION AND BUILDING MATERIALS, 304, 1-13 [10.1016/j.conbuildmat.2021.124486].

Availability:
This version is available at: https://hdl.handle.net/11585/841973 since: 2024-07-16

Published:

DOI: http://doi.org/10.1016/j.conbuildmat.2021.124486

A staggered multiphysics framework for salt crystallization-induced damage in porous building materials

G. Castellazzi[1,*], A.M. D'Altri, S. de Miranda, H. Emami, L. Molari, F. Ubertini
ALMA MATER STUDIORUM - University of Bologna - DICAM - Viale del Risorgimento

---

Abstract

In this paper, a staggered multiphysics framework is proposed for the numerical simulation of salt crystallization-induced damage in porous building materials, such as masonry. This staggered framework is based upon a multiphase model to account for salt transport and crystallization within the porous material and a plastic-damage model to account for the nonlinear mechanical behavior of the material. The staggered structure is composed of a two-way data exchange between the multiphase and the mechanical models. Firstly, crystallization pressure information is passed to the mechanical model to analyze the mechanical response of the material. Secondly, the mechanical outcomes (e.g. damage distribution) are used to update some multiphase model properties (e.g. tortuosity) allowing simulations also beyond the onset of damage. Few simple geometry-based relationships are discussed to update multiphase model properties along with damage. Numerical examples are used to show the capability of the proposed staggered framework for simulating complex interactions among salt transport, salt crystallization, and damage within the porous material, highlighting the possibilities of this modeling approach to conduct simulations also beyond the onset of damage.

Keywords: Multiphase model, Damage, Pore pressure, Spalling, Salt crystallization, Staggered solution, porous materials, masonry.

---

[*] giovanni.castellazzi@unibo.it

Postprint version - https://doi.org/10.1016/j.conbuildmat.2021.124486

1. Introduction

Environmental actions, which are likely to get worse in the future according to climate change predictions [1], can give rise to degradation processes and aging in historic building materials, such as masonry [2]. One of the main threats to degradation of porous building materials is salt crystallization [3, 4]. Indeed, salt crystallization-induced damage in porous building materials can affect the structural performance of existing buildings [5] and the effectiveness of strengthening systems applied on them [6], [7].

In the last decades, a large amount of experimental and theoretical research was dedicated to study the transport of dissolved salt in porous materials [8, 9, 10, 11], salt phase change [12, 13, 14], and pore pressure which results from salt crystallization [12, 15, 16, 17].

Differently from laboratory tests which can typically deal with small-scale specimen and relatively short-terms weathering conditions (whose representativeness of in situ environment is still object of debate [18]), numerical strategies can potentially simulate long-term real-life conditions also on large- and full-scale structures. To this aim, several numerical models have been developed in the last years. In [19], a chemo-hydro-thermo-mechanical model for salt transport and crystallization in porous building materials has been presented considering a linear elastic response of the material matrix. An extension of this model to damage has been discussed in [20], where the spalling in masonry due to salt crystallization has been investigated up to the onset of damage. Derluyn et al. [21] developed a coupled model for heat and mass transport, salt crystallization, deformation and damage able to identify crack nucleation by comparing the effective stress and the tensile strength. Additionally, part of the Authors developed in [22], [23], [24] a coupled multiphase model for the hygro-thermal analysis of masonry structures and prediction of stress induced by salt crystallization. Particularly, this model allowed the simulation of an aging test conducted on a masonry wall exposed to long-term weathering conditions. Such model has been successively extended in [25], where a multi-scale approach for the analysis of mechanical effects induced by salt crystallization in porous media has been developed through the real 3D micro geometry of the porous material and using a linear elastic material mechanical behavior. Lately, Choo &

Sun [26] developed a coupled multiphase and phase-field model to investigate cracking and damage from crystallization in pores. This coupled strategy enables simulation of complex fractures in the porous material without explicitly tracking their geometry, allowing the simulation up to the onset of cracking and damage from in-pore crystallization of minerals. A common drawback of this state-of-the-art resides in the limitation of the numerical simulations up to the onset of damage, as many assumptions in the constitutive models break down upon damaging of the material.

In this paper, a staggered multiphysics framework is proposed for the numerical simulation of salt crystallization-induced damage in porous building materials, such as masonry. This staggered framework is based upon a multiphase model to account for salt transport and crystallization within a porous material [22] and a plastic-damage model to account for the nonlinear mechanical behavior of the material [27].

A two-way staggered framework allows for the data exchange between the multiphase and the mechanical models: pore pressure information is passed to the mechanical model to analyze the mechanical response of the material; subsequently, the damage distribution obtained from the mechanical response is used to update some multiphase model properties allowing simulations also beyond the onset of damage. Few simple geometry-based relationships are discussed to update multiphase model properties along with damage.

The paper is organized as follows. Section 2 highlights the main aspect of the staggered multiphysics framework herein presented. The multiphase model for salt transport, diffusion and crystallization is briefly recalled in Section 3. Section 4 presents the main aspect of the mechanical model. Section 5 illustrates the strategy for the updating of the multiphase model properties within the staggered framework. Section 6 shows the structure of the staggered framework. Numerical results are presented and discussed in Section 7. Section 8 discusses the conclusions of this research work.

2. Multiphysics staggered framework

In this paper, the multiphase model (MPM) presented in [22] for the salt and crystallization is coupled with a mechanical model (MM) through a staggered multiphysics framework to account for the damage induced by salt crystallization. The structure of the coupled problem is sketched in Figure 1: at a generic step, the distributions of the crystallization pressure and of the saturation degree of crystallized salt, predicted by the multiphase model, are used as input data for the nonlinear mechanical model. This, gives in turn the distribution of the damage in the solid matrix of the porous material as output. Finally, the damage variable is used to update some of the multiphase model parameters. In this regards, in the following the attention is focused only on the tortuosity, for simplicity. However, it is worth to note that the list of the parameters of the multiphase model to be updated can be easily enriched without substantially altering the proposed framework.

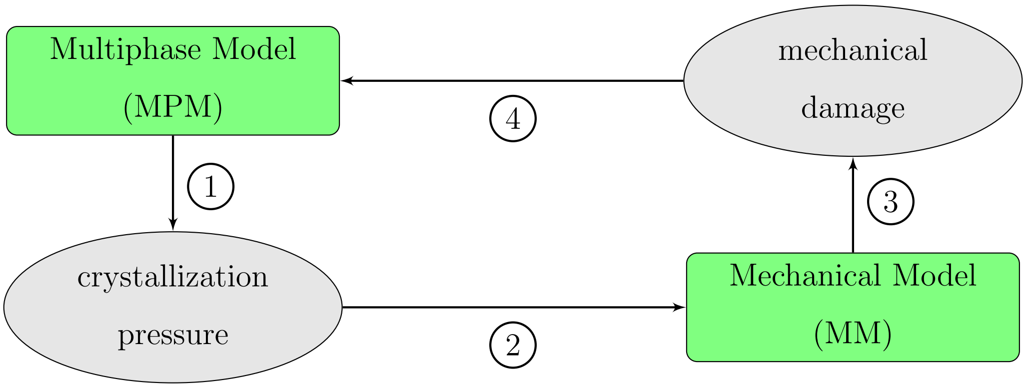

Figure 1: Sketch of the coupled multiphysics model.

The tortuosity τ is defined as the ratio of the effective length L_e to the direct length L of a path that connects two points A and B of a porous material. It is considered to vary during an evolutive analysis not only due to the change in porosity, ϕ, resulting from the crystallized salt, but also due to the evolution of mechanical damage, as sketched in Figure 2. In particular, as illustrated in Figure 2b, precipitated salt crystals change the porosity ($\phi_1 < \phi_0$) and the pore geometry resulting in an increase of effective length ($L_{e1} > L_{e0}$) and, hence, in an increase of the tortuosity ($\tau_1 > \tau_0$). Moreover, as illustrated in Figure 2c, if the

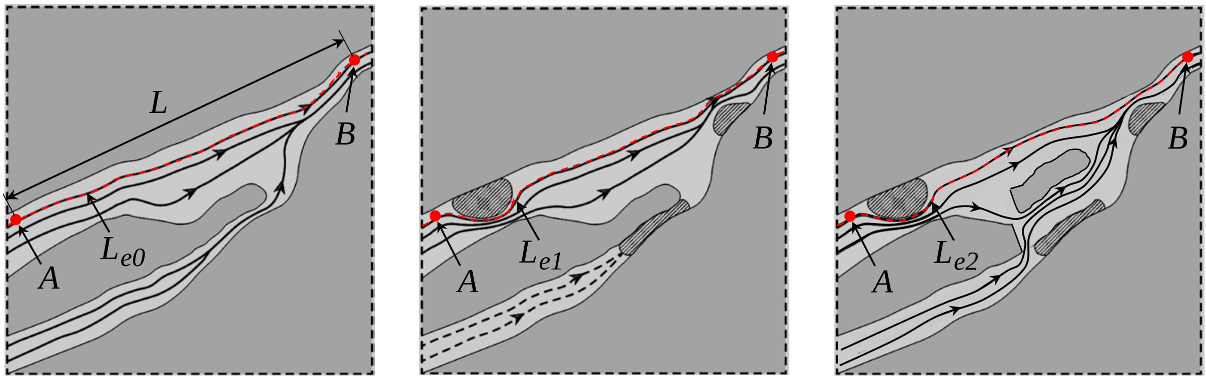

(a) Initial condition: undamaged porous material L_{e0}, ϕ_0, τ_0.

(b) Undamaged porous material with precipitated salt crystals L_{e1}, ϕ_1, τ_1.

(c) Porous material damaged by crystallization pressure L_{e2}, ϕ_1, τ_2.

Figure 2: Salt crystallization-induced evolution of porosiy and tortuosity of the porous material.

damage of the porous material is activated by the crystallization pressure, a further change may occur in the effective length and, therefore, in the tortuosity.

Obviously, in addition to the coupling between the two models, inside each model some of the parameters are updated during the analysis. Inside the MPM, some parameters are function of internal variables of the model itself (e.g. the porosity is updated according to the saturation degree of crystallized salt). Analogously, some parameters of the mechanical model are updated during the analysis as a function of internal variables of the mechanical model itself (e.g. the elastic properties are updated according to the level of damage).

From a phenomenological point of view, the above-mentioned phenomena (i.e. crystallization process and damaging process) possess different time scale: the first has a slow evolution characterized by long time units (days, months, years); the latter has a fast evolution, characterized by short time units (seconds, minutes, hours).

This is certainly one of the main motivations of using a staggered solution scheme which allows to exchange the data periodically, at defined time intervals Δt. In this regards, here we propose a special staggered framework to solve the coupled problem and track the salt crystallization-induced damage within the porous material, whose organization is sketched in Figure 3. In particular, the proposed staggered solution has been implemented in two versions to foster comparisons: one-way coupling (Figure 3a), and two-way coupling

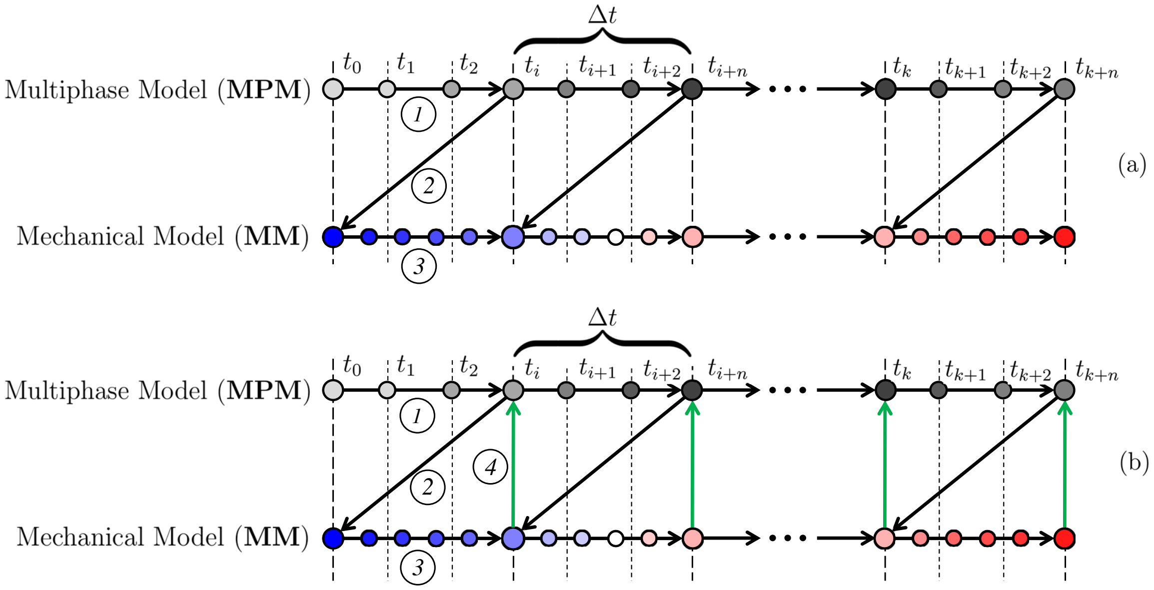

Figure 3: Staggered scheme. One-way coupling (a); two-way coupling (b).

(Figure 3b). In the first case, the multiphase model is solved at time t (step 1); then, pore pressure information is passed to the mechanical model (step 2); the mechanical response of the material is solved (step 3). In the second case, a further step is performed and the mechanical damage distribution is used to update the tortuosity τ (step 4).

Another motivation to adopt a staggered resolution scheme is related to its computational convenience and convergence. Indeed, the separate solution of each problem appears particularly convenient in terms of computational cost and more robust with respect to the case of a monolithic scheme of such a nonlinear problem [28].

3. Multiphase model for salt transport and crystallization

In this section, the multiphase model for salt transport and crystallization developed in [22] is briefly recalled. The porous material is considered as a multiphase medium, which consists of the skeleton and voids, that may be partly filled with moist air, salt dissolved in solution and/or salt crystals, see Figure 4. We apply here a macroscopic formulation that makes use of a representative elementary volume (REV) of a porous medium, large enough to include all the phases present. Moreover, the region is assumed to be of sufficient size that the average values that characterize a phase are independent of that size [29]. Mass exchange between different phases might arise (i.e. water evaporation, salt crystallization/dissolution), as well as the interaction between the fluid phases and the skeleton.

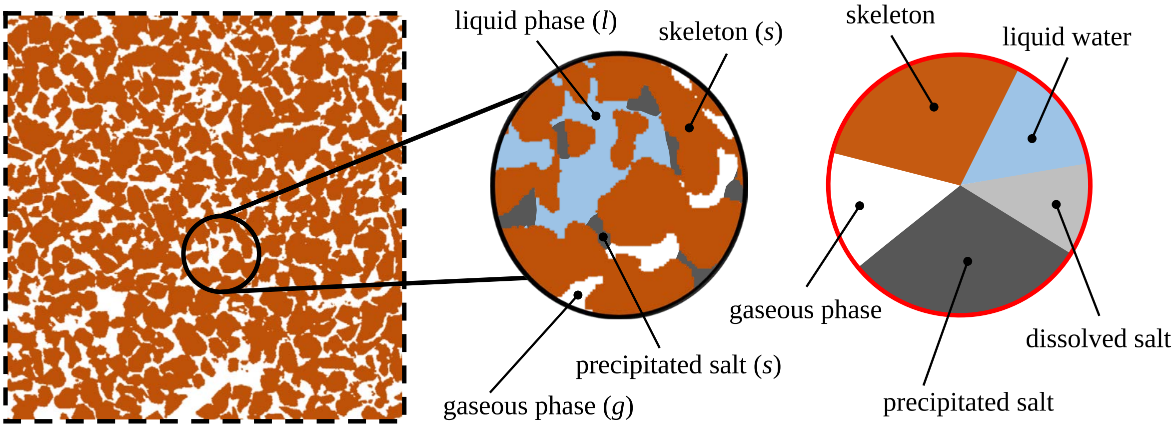

Figure 4: Porous medium: Representative Elementary Volume (REV) of a four-phase mixture composed of the solid matrix (s), liquid solution(l), gas (g), and precipitated salt (s).

The content of each component is described by the concentration c_α^π, defined as the mass of α in π-phase per unit volume of porous material, or by the corresponding saturation degree S_α^π, defined as the pore volume occupied by α in π-phase. The concentration c_α^π and the corresponding saturation degree S_α^π are related as $c_\alpha^\pi = (\phi_0 \cdot S_\alpha^\pi) \cdot \rho_\alpha^\pi$, where ρ_α^π is the mass density of α in π-phase.

Assuming isothermal conditions, the independent variables assumed to describe the phenomenon are the pore relative humidity h (the vapor pressure divided by the vapor pressure at saturation) and the mass fraction of dissolved salt ω:

$$\omega = \frac{c_s^l}{c_w^l + c_s^l} \tag{1}$$

being c_s^l the concentration of salt in liquid phase and c_w^l the liquid water concentration. These independent variables are supplemented by the internal variable c_s^s (concentration of crystallized salt).

3.1. Balance equation

With reference to the REV illustrated in Figure 4, the mass balance equations of moisture and salt can be written as:

$$\frac{\partial c_w}{\partial t} + \nabla \cdot \mathbf{j}_w = -\mu_w^{ls} \tag{2}$$

$$\frac{\partial c_s^l}{\partial t} + \nabla \cdot \mathbf{j}_s^l + \frac{\partial c_s^s}{\partial t} = 0 \tag{3}$$

where c_w is the concentration of moisture (defined as the sum of liquid water concentration c_w^l and the vapor water concentration c_w^g), $\mathbf{j}_w$ the moisture flux (defined as the sum of water vapor and liquid water flux: $\mathbf{j}_w = \mathbf{j}_w^g + \mathbf{j}_w^g$), and μ_w^{ls} the rate of liquid water trapped in hydrated salt crystals. The fluxes of liquid water and dissolved salt can be expressed in terms of ω as:

$$\begin{aligned} \mathbf{j}_w^l &= (1-\omega)\mathbf{j}_{ws}^l - \mathbf{j}_{s,\mathit{diff}}^l \\ \mathbf{j}_s^l &= \omega \mathbf{j}_{ws}^l + \mathbf{j}_{s,\mathit{diff}}^l \end{aligned} \tag{4}$$

where $\mathbf{j}_{ws}^l$ is the flux of the liquid phase and $\mathbf{j}_{s,\mathit{diff}}^l$ is the diffusive flux of dissolved salt.

3.2. Constitutive equations

The constitutive equations can be written as:

$$\mathbf{j}_w^g = -\frac{D_v}{R_v T}\nabla p_v \tag{5}$$

$$\mathbf{j}_{ws}^l = -g_\omega(\omega) D_l \left(S_w^l\right)^{n_l} \nabla p_c \tag{6}$$

$$\mathbf{j}_{s,\mathit{diff}}^l = -\rho_{ws}^l \frac{D_s}{\tau} f_s\left(S_w^l\right) \nabla \omega \tag{7}$$

where p_v the vapor pressure, p_c the capillary pressure, ρ_{ws}^l the mass density of the liquid phase, R_v is the gas constant of water vapor and D_v the vapor permeability coefficient. The exponent n_l ranges from 1 to 6 as suggested by [19] and D_l is the liquid conductivity of pure water [30]:

$$D_l = \left[3.8\left(\frac{A}{\phi_0 \rho_w^l}\right)^2 10^{3\left(S_w^l - 1\right)}\right] \frac{\partial c_w}{\partial h} \tag{8}$$

being A the water adsorption coefficient, ρ_w^l the mass density of liquid water and S_w^l the degree of saturation of the solution. Moreover, in agreement with [31] the expression $g_\omega =$

$\frac{\rho^l_{ws}}{\rho^l_w}(1-0.03m)$ is assumed, being m the molality.
For the salt diffusion part, D_s is the diffusion coefficient for pure water and $f_s = (S^l_w)^{n_s}$ is a correction factor that takes into account the actual cross section available for diffusion, and n_s is the saturation exponent, here set equal to one.

As anticipated in Section 2, when the salt precipitates the porosity tends to decrease due to the voids occupied by the salt. This phenomenon is taken into account in the model by introducing the effective porosity:

$$\phi_{eff} = \phi_0(1 - S^s_s) \tag{9}$$

where S^s_s is the crystallized salt saturation degree. Moreover, as described in Section 2, the porosity change due to salt crystallization can alter also the tortuosity and, hence, the salt diffusion. Several expressions which relate tortuosity and porosity can be found in the literature [32, 33, 34, 35, 36, 37, 38, 39]. Here, we refer to the relationship provided in [33, 37, 40]:

$$\tau = 1 - p \ln(\phi_{eff}) \tag{10}$$

Varying coefficient p, the above expression can be applied to a bed of uniform spheres as well as to overlapping, non-uniform spheres, see Figure 5.

In this model, the instantaneous equilibrium between liquid and vapour water is assumed. Accordingly, the moisture content at a certain temperature can be expressed as a function of the relative humidity. This relation, known as sorption/desorption isotherm, can be considered as a material property and can be obtained by experimental testing, see for instance [41] and the reference therein. The sorption isotherm is commonly determined for pure water, but it is influenced by the dissolved salt due to of the changing contact angle and the surface tension of the solution [42], and can be conveniently expressed in terms of saturation degree of the solution S^l_{ws} as a function of the equivalent relative humidity. In particular, the analytical expression for sorption/desorption curves proposed in [30] is here adopted:

$$S^l_w = \frac{\psi - 1}{\psi - h} h \tag{11}$$

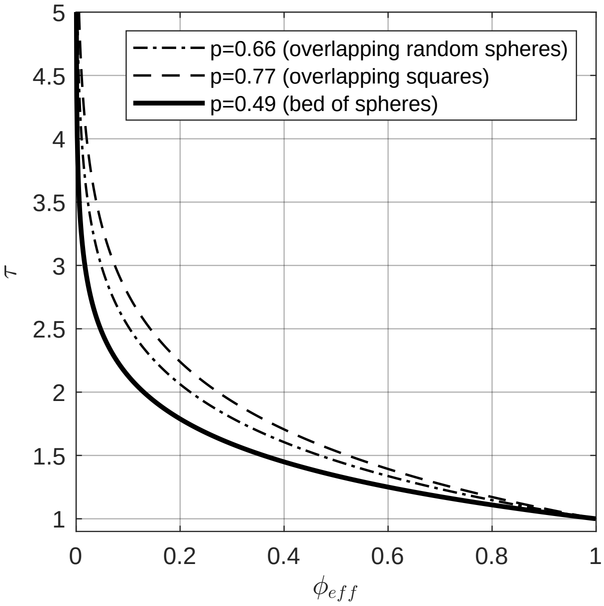

Figure 5: Effect of effective porosity variation on tortuosity for different values of p

where ψ is the sorption isotherm parameter. Then, the relation for sorption curves takes into account for the presence of precipitated salt inside the pores and, indirectly, the effect of the presence of dissolved salt, see also [22][43] for further details.

3.3. Crystallization and dissolution equations

The salt crystallization or dissolution depends on the supersaturation ratio which is defined by the ratio ω/ω_{sat}, being ω_{sat} the dissolved salt concentration at saturation. In particular:

$$\begin{cases} \frac{\omega}{\omega_{\text{sat}}} > \alpha_0 \;\Rightarrow\; \text{crystallization} \\ \frac{\omega}{\omega_{\text{sat}}} < 1 \quad\;\Rightarrow\; \text{dissolution} \end{cases} \tag{12}$$

where α_0 is the crystallization threshold ($\alpha_0 > 1$ for first crystallization, $\alpha_0 = 1$ for further crystallization). In general, the threshold of supersaturation ratio for primary crystallization relies on the properties of the porous material and on the type of salt. The evolution equation which describes the salt precipitation/dissolution kinetics, i.e. quantifies the amount of salt which precipitates, can be written as:

$$\frac{\partial c_s^s}{\partial t} = \pi r_p^2 \rho_s^s \frac{n}{V_{tot}} K_c \left| \frac{\omega}{\omega_{sat}} - 1 \right|^P \tag{13}$$

where a constant amount of salt nuclei n in the solution, as well as an isotropic distribution of cylindrical pores and cylindrical nuclei of the same radius of the pores (r_p), is assumed. In Equation (13), ρ_s^s is the density of the crystallized salt, K_c is the growth rate coefficient, V_{tot} the pore volume and P is the crystallization process order that relies on the properties of the porous material and on the type of salt. As noted in [44] in the case of nitrates, the crystallization-dissolution process could be described using an improved model incorporating Pitzer's equations.

3.4. Crystallization pressure

When the salt crystallizes inside the pores it exerts a pressure on the solid matrix that can be evaluated with the well-known relation introduced by Steiger in [13]:

$$p_s = \frac{vRT}{V_s}\left(\ln\frac{\omega}{\omega_{sat}} + \ln\frac{\gamma}{\gamma_{sat}}\right) \tag{14}$$

in which v is the total number of ions released due to complete dissociation of salt, R is the ideal gas constant, T is the temperature, V_s is the molar volume of precipitated salt, γ is the mean activity coefficient of the dissolved salt and γ_{sat} is the mean activity coefficient of the dissolved salt at saturation. As noted in [45], when the porous material is characterized by high values of pore size (e.g. in natural stones), Eq. (14) could be extended to account for the influence of pore size on the solution properties.

4. Mechanical model

As for the mechanical model, a continuum body is considered. The compatibility equation is written as:

$$\boldsymbol{\varepsilon} = \frac{1}{2}(\nabla\mathbf{u}^T + \nabla\mathbf{u}) \tag{15}$$

being $\mathbf{u}$ the displacement vector and $\boldsymbol{\varepsilon}$ the strain tensor. Given the small velocities of the phases, the equilibrium reads:

$$div(\boldsymbol{\sigma}) + \boldsymbol{F} = 0 \tag{16}$$

where $\boldsymbol{\sigma}$ is the stress tensor and $\boldsymbol{F}$ the vector of volume forces, which, if no external distributed loads are prescribed, can be written as:

$$\boldsymbol{F} = \boldsymbol{g}\rho_{eff} \tag{17}$$

being $\boldsymbol{g}$ the gravitational acceleration vector and ρ_{eff} the effective mass density defined as:

$$\rho_{eff} = \rho_m + c_w^g + c_w^l + c_s^l + c_s^s \tag{18}$$

being ρ_m the mass de5nsity of the solid matrix.

Isotropic material behavior based on the plastic-damage model developed by Lee and Fenves [27] is considered. Particularly, this constitutive law aims to phenomenologically represent the mechanical response of quasi-brittle materials, such as brick. In this framework, the constitutive relationship is expressed as:

$$\boldsymbol{\sigma} = (1 - D)\mathbb{C}(\boldsymbol{\varepsilon} - \boldsymbol{\varepsilon}_p) - \boldsymbol{\sigma}_s \tag{19}$$

where D is the scalar degradation damage variable, $\mathbb{C}$ is the initial undamaged elastic stiffness tensor, $\boldsymbol{\varepsilon}_p$ is the plastic part of the strain tensor and $\boldsymbol{\sigma}_s$ accounts for the stress induced by salt crystallization.

To account for the different behavior of the quasi-brittle material in tension and compression (i.e. cracking in tension and crushing in compression) within a plastic-damage framework, two independent scalar damage variables ($0 \leq d_t < 1$ for tensile regime and $0 \leq d_c < 1$ for compressive regime) are considered in the constitutive model. Indeed, it should be herein highlighted that a combination of cracking/crushing failure modes can be expected also due to the stress induced by salt crystallization. Accordingly, the damage state of a single material point can be overall represented by the single degradation damage variable D expressed as:

$$D = 1 - (1 - d_t)(1 - d_c) \tag{20}$$

which combines tensile and compressive damage states.

It can be easily verified that D in (20) fulfills the condition $0 \leq D < 1$ and is equal to either d_t

when $d_c = 0$ (tensile case) or d_c when $d_t = 0$ (compressive case). This constitutive law adopts the concepts of isotropic degradation damage, strain decomposition and effective stress, i.e. from both damage mechanics and plasticity theories, see Eq. (21). A nonassociative flow rule, obtained by a Drucker-Prager type plastic potential is considered, is considered to govern the dilatancy and to define the plastic strain rate. The flow rule is controlled by the dilatancy angle ψ, generally assumed equal to 10°in agreement with physical evidence and previous computational approaches, and a smoothing constant ϵ typically assumed equal to 0.1. Furthermore, a multiple-hardening Drucker-Prager type surface is adopted as yield surface. This surface is governed by the ratio f_{b0}/f_{c0} between the biaxial initial compressive strength f_{b0} and the uniaxial initial compressive strength f_{c0} and a constant ρ, which represents the ratio of the second stress invariant on the tensile meridian to that on the compressive meridian at initial yield. Generally, $f_{b0}/f_{c0} = 1.16$ and $\rho = 2/3$ for quasi-brittle materials, such as brick. The general parameters adopted for brick are collected in Table 1.

ϵ	ψ	f_{b0}/f_{c0}	ρ
0.1	10°	1.16	2/3

Table 1: General parameters for the brick plastic response

As regards the stress induced by salt crystallization, collected in $\boldsymbol{\sigma}_s$, it should be noted that, basing on the so called Law of Partial Pressures [46], $\boldsymbol{\sigma}_s$ can be evaluated as:

$$\boldsymbol{\sigma}_s = \boldsymbol{I}\sigma_s = \boldsymbol{I} b S_s^s p_s \tag{21}$$

where b is the Biot's coefficient and $\boldsymbol{I}$ is the identity operator.

5. Updating of multiphase model parameters

We now specify how the damage induced by the salt crystallization affects the multiphase model parameters. In particular, as anticipated in Section 2, the attention is herein focused on the tortuosity which is herein assumed to be dependent on the actual mechanical damage D. Accordingly, Equation (7) is updated along with the current state of damage, leading to an updating of the multiphase model. For the tortuosity update, we assume a law analogous to that used for lithium-ion battery electrodes, where the underlying microstructural tortuosity controls the macroscopic charge capacity, average lithium-ion diffusivity, and macroscopic resistivity of the cell [47]. Then, the Equation (7) is updated by means of the following definition of the effective tortuosity parameter:

$$\tau_{eff}(D) = \tau \cdot \beta_\tau(D) \tag{22}$$

where β_τ is the tortuosity damage function that describes how tortuosity evolves along with damage in the porous structure.

In order to infer the β_τ function, we suppose here the porous material as a bed of spheres (Figure 6). If we consider that for a specific region of interest (see Figure 6a), we reach a level of crystallization pressure capable to induce damage, then, we can assume a local change of τ according to the evolution of the simplified pore structure. With this in mind, we consider the scenario illustrated in Figures 6a-6d: for increasing damage, β_τ increases until the damage reaches a certain thershold value D^* ($\beta_\tau = \beta_{\tau,1}$ for $D = D^*$) and then decreases till specific value $\beta_{\tau,2}$ defined by the evolution of the particle size.

A possible evolution of β_τ, along with the damage variable D, is described in Figure 6(e): we use the smooth-stepping function to modulate the value of β_τ along the variation of the damage variable D with reference to the damage threshold level D^*:

$$\beta_\tau(\beta_{\tau,1}, \beta_{\tau,2}, D, D^*) = \begin{cases} 1 + (\beta_{\tau,1} - 1)(\frac{D}{D^*})^2(3 - \frac{2D}{D^*}), & \text{for } D = [0, D^*] \\ \beta_{\tau,1} - (\frac{D-D^*}{1-D^*})^2(3 - 2(\frac{D-D^*}{1-D^*}))(\beta_{\tau,1} - \beta_{\tau,2}), & \text{for } D = [D^*, 1] \end{cases} \tag{23}$$

In general, we can consider that $\beta_{\tau,2}$ could be precomputed in order to fulfill the following constrain:

$$\tau_{eff} = \tau\beta_\tau = 1 \qquad \text{if} \quad D = 1 \tag{24}$$

6. Computational method for the staggered solution

We now detail the implementation of the staggered framework sketched in Figure 3 for the solution of the coupled multiphysics problem.

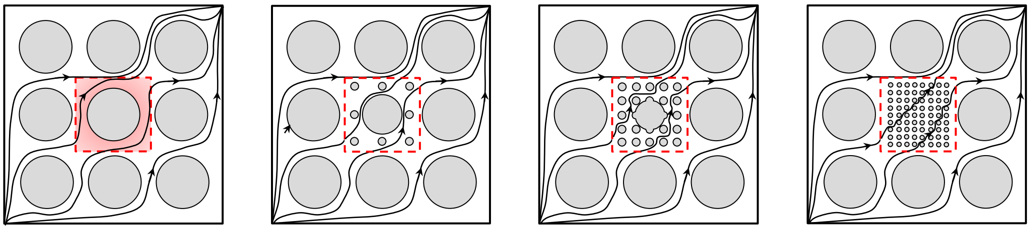

(a) undamaged (b) damaged below D^* (c) damage at D^* (d) damaged over D^*

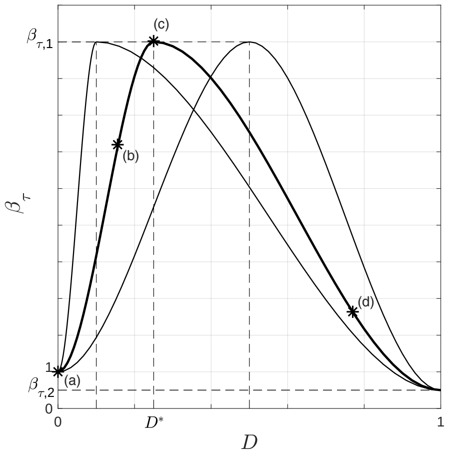

(e) evolution of β_τ function

Figure 6: Tortuosity update due to mechanical damage.

6.1. Space discretization

In order to implement the model, the domain is discretized in space using the finite element method for the salt transport and crystallization problem and for the mechanical problem. The proposed staggered procedure allows for the use of different meshes when exchanging informations between MPM and MM.

6.2. Fields transfer operation strategy

According to the pseudo-code reported in Algorithm 1 and illustrated in Figure 3 (steps 1, 2, 3, and 4 of Figure 3 are highlighted in Algorithm 1 too), the proposed staggered technique could admit some variants depending on the different use of the Fields Transfer Operation (FTO) between the two sets of field equations. These operations (namely step 2 and step 4 of the algorithm 1) can be run at every time step in each field, or can be optimized based on the different evolution times of MPM and MM. In particular, the effect of

```
Algorithm 1: Pseudo-code of the required steps to run the staggered solution
    Input: $\phi_0$, $\tau_0$, $\omega_{sat}$, $\Delta t$, $D^*$, $D$ and set $n = 1$
    Output: $c_s^s$, $S_s^s$, $\boldsymbol{\sigma}$, $D$, $\phi_{eff}$, $\tau_{eff}$
①   MPM - Compute/Update $\phi_{eff}$, $\tau_{eff}(\phi_{eff},\ D)$, $p_s$
    if $t = n\Delta t$ then
        $n = n + 1$
②       FTO → from MPM to MM
            $\boldsymbol{\sigma}_s = \boldsymbol{I}\sigma_s = \boldsymbol{I}bS_s^s p_s$
③       MM
            Compute/Update $D$
④       FTO → from MM to MPM
            Compute/Update $\beta_\tau(\beta_{\tau,1}, \beta_{\tau,2}, D, D^*)$
    else
        $t = t + 1$
    end
    Repeat Steps 1 to 4, till $t = t_{final}$
```

the choice of the time interval Δt between two FTO has been investigated, see Appendix A.2.

7. Numerical examples

The multiphase model is applied to evaluate the effects of the mechanical coupling on the salt transport and crystallization processes in a benchmark consisting in a fired clay masonry panel exposed to specific boundary conditions, inspired by the benchmark analyzed in [20]. To this aim, we analyze a portion of the panel representative for a generic region of interest, as illustrated in Figure 7: we consider a generic transverse section of the panel (see cutting plane Π_0) and focus the attention on a small portion of it depicted in Figure 7.

In the following, we use the same mesh to solve the fields variables of both models but with finite elements of different order: the primary variables of the multiphase model, h and ω, are interpolated based on Lagrangian shape functions adopting standard 9-node

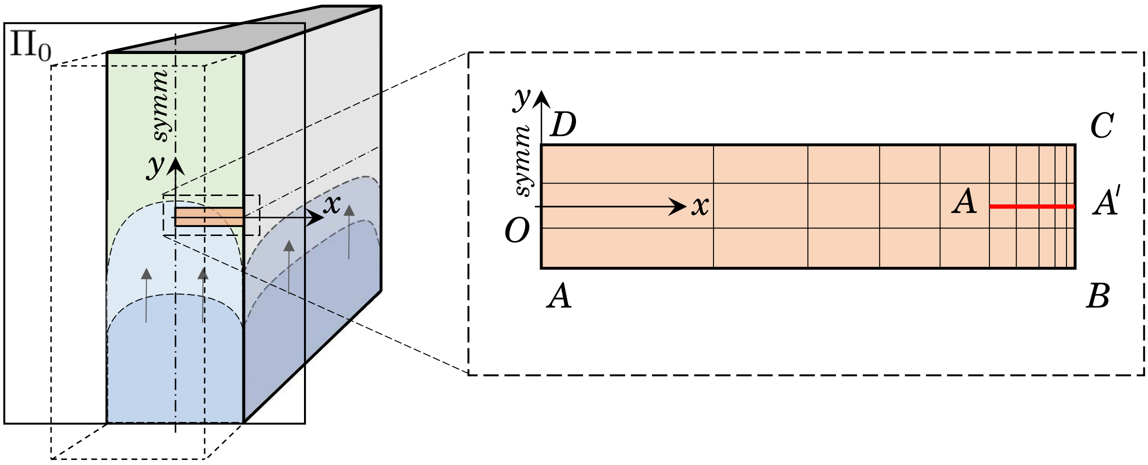

Figure 7: Illustration of the boundary conditions over a region of interest on the cutting plane Π_0: $\overline{DC}$ and $\overline{AB}$ no flux, $u_y = 0$; $\overline{AD}$ prescribed relative humidity $\overline{h}$ and prescribed mass concentration of dissolved salt $\overline{\varpi}$ and symmetry boundary condition for the displacement field; $\overline{BC}$ allowed evaporation with prescribed environmental humidity. The cutting line $A - A'$ highlighted in red color.

elements; the mechanical primary variable, the displacement, is also interpolated based on standard Lagrangian shape functions but adopting 4-node elements. Mesh is constructed using $N_x = 3$ and $N_y = 100$ elements along the directions x and y, respectively, using a 0.1 element ratio biasing along the x direction (a mesh sensitivity analysis has been also conducted and the main results are collected in Appendix A.1).

The time slot Δt, that rules the FTO, has been set equal to $\Delta t = 6$ hours (the sensitivity to the FTO time interval has been tested for several Δt values and the main results are collected in Appendix A.2).

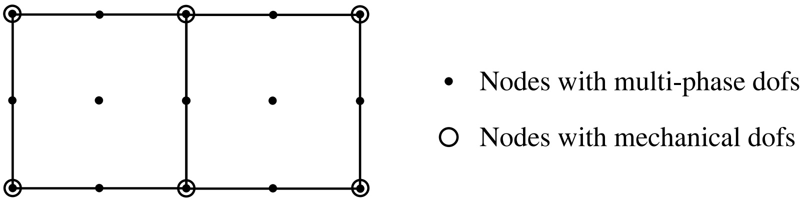

Figure 8: An example mesh illustrating the location of finite element degrees of freedom. Note that linear element and quadratic element can be employed for modeling the two problems.

7.1. Benchmarks definition

Three specific numerical setups are considered and they are organized as follows:

BM#1 In this case, no tortuosity update is considered [22] (i.e. the tortuosity is set constant $\tau = 1$). FTOs are set according to Figure 3(a), using therefore a one-way coupling framework.

BM#2 An extension of the MPM in [22] is used in this case to solve the problem, updating the tortuosity as function of the effective porosity with the relation provided for bed of spheres defined using $p = 0.49$ in Equation (10). Hence, the constitutive law in Equation (7) is updated in time through the definition of the salt diffusion coefficient: an increase of tortuosity will correspond to a drop of the diffusive flux of dissolved salt. The results are illustrated tracking in time variables as for BM#1 plus the tortuosity variable $\tau(\phi_{eff})$. FTOs are set according to Figure 3(a), using therefore a one-way coupling framework.

BM#3 This case implements the full coupling of the MPM and MM along the evolution in time: the tortuosity is updated along with the effective porosity and the mechanical damage using Equations (22) and (23) setting $\beta_{\tau,1} = 2$, $\beta_{\tau,2} = 1$ and $D^* = 0.2$. Results are illustrated tracking in time variables as for BM#2. FTOs are set according to Figure 3(b), using therefore a two-way coupling framework.

For each benchmark we consider 96 hours simulations along with the following Environmental Boundary Conditions (EBC) aimed at simulating a portion in time of an ideal weathering real cycle: constant environmental humidity $h_{env} = 50\%$ on $\overline{BC}$ (see Figure 7), initial porous material humidity equal to 50%, on $\overline{AD}$ prescribed humidity $\overline{h}$ that rises from 50% to 99,6% in few hours and prescribed mass concentration of dissolved salt $\overline{\omega} = 0.04$ (see Figure 7). As regards the MPM, material properties are set according to [48], and sodium chloride (NaCl) is chosen as salt present in the saline solution. Summary of the model parameters is reported in Table 2. The crystallization process order P appearing in the growth rate law in

Equation (13) is set equal to one, as typically used for sodium chloride salt [48]. Nevertheless, a further numerical investigation has been conducted, see Appendix A.3, to test the robustness of the proposed procedure in case of different salts with different crystallization process order P that rules the growth rate law in Equation (13). Obtained results show a significant stability of the proposed method.

The time discretization is carried out by means of the backward finite difference method. A standard iterative strategy based on the Newton–Raphson method is applied to solve the MPM non-linear system of equations [49].

The MM is defined using the following mechanical material parameters for masonry $E = 1.8GPa$ and $\nu = 0.2$. Being the model formulated in the context of non-associated plasticity [27], the plastic potential is defined by the dilatancy angle ψ, assumed equal to $10°$ as generally done for masonry, as well as by a smoothing parameter ϵ assumed equal to 0.1. In addition, the strength domain is specified by the ratio f_{b0}/f_{c0} between the biaxial f_{b0} and uniaxial f_{c0} initial compressive strengths, assumed equal to 1.16, and by the shape constant ρ_D, assumed equal to 2/3 [27]. Compressive strength is set equal to $f_c = 2.0MPa$ and the tensile strength is set equal to $f_t = 0.12MPa$.

7.2. Results discussion

The discussion of the results is carried out by a direct comparison of the outcomes for benchmarks BM#1, BM#2 and BM#3 in Figure 9 and Figure 10. In these figures, results are illustrated tracking in time the following fields variables: humidity h, supersaturation ratio ω/ω_{sat}, degree of saturation of crystallized salt S_s^s, tortuosity τ, stress σ_s and degradation damage variable D along the cutting line $A - A'$ (where salt crystallization mainly occurs), as described in Figure 7. As expected, the rapid variation of the humidity near the evaporating surface ($\overline{BC}$ boundary in Figure 7), shown in Figure 9(a), leads to an increase of the supersaturation ratio, see Figure 9(b). In particular, by inspecting Figure 9(b) it is possible to note that, for all the setups, after $t = 24$ hours, the triggering condition of Equation (12) will cause salt precipitation near the surface $\overline{BC}$. This is confirmed by Figure 10(a) and (c) showing an increase of the saturation degree S_s^s and of the stress σ_s in the

	Quantity	Value	Units	Source
K_c	Growth rate coefficient	0.03	$\mu m/s$	[50][51]
n	Nuclei in solution	4×10^{-6}	$(\mu m^3)^{-1}$	[52]
ϕ_0	Initial porosity	26%	–	[22]
ω_{sat}	Concentration of dissolved salt at saturation	0.264	kg/kg	[22][24][53]
D_v	Vapor permeability coefficient	0.0039	m^2/h	[30]
α_0	Crystallization threshold	1	–	[52]
ρ_s^s	Salt NaCl density	2160	kg/m^3	Literature
r_p	Mean pore radius	0.700	μm	[22]
A	Water adsorption coefficient	0.185	$kg/m^2/s^{0.5}$	[22]
K_s	Salt diffusion Coefficient	0.499×10^{-9}	m^2/s	[22]

Table 2: Summary of the model parameters used in the numerical tests.

same zone (the stress σ_s are computed ad a post-process of the MPM results using Equation (21)). In particular, for the BM#1 the stress concentrates near $x = 1.1918$ (highlighted through a vertical dotted line in Figures 9 and 10) with a maximum magnitude equal to $\sigma_s = 10.0MPa$ for $t = 60$ hours. Furthermore, it is interesting to note that for BM#1 after $t = 60$ hours the S_s^s increases whether, due to the decreasing supersaturation ratio, the σ_s is decreasing too. Moreover, it is worth to note that for BM#1 the single degradation damage variable D, shown in Figure 10(d), remains equal to zero during the whole simulated time.

Differently, the effective description of the tortuosity, introduced for BM#2 and BM#3, leads to an update of the various quantities (the stress is now characterized by an increased peak value of $16.5MPa$ and of $18.3MPa$ at $t = 36$ hours for the BM#2 and BM#3 setups, respectively) but, above all, to the activation of the mechanical damage. In particular, inspecting Figure 10(c) and (d), it can be noted that for BM#2 and BM#3 after $t = 36$ hours the stress decreases, due to damage activation (in the zone near $x = 1.1918$, D passes from 0.18 at time $t = 36$ hours to about 0.92 at $t = 96$ hours). Furthermore, it appears worth to note that, for BM#3, the tortuosity drops where the damage variable exceeds the

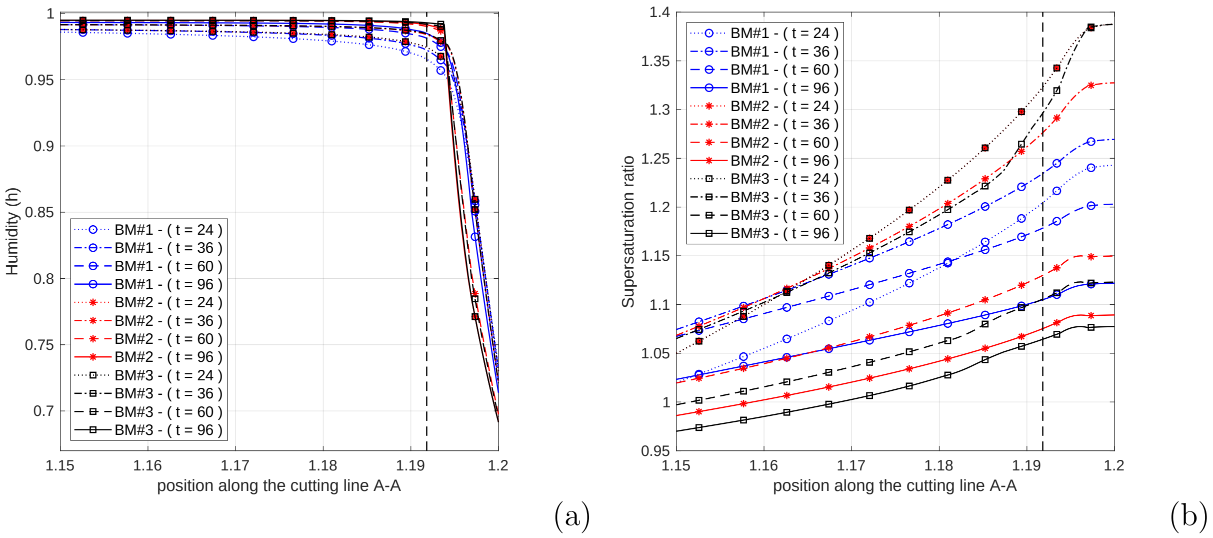

Figure 9: Benchmarks results comparison: illustration of fields variation for $t = [24, 36, 60, 96]$; humidity h (a), supersaturation ratio ω/ω_{sat} (b).

threshold $D^* = 0.2$, according to the full coupling of the FTO that admits the combined evolution of fields. Finally, it should be noted that for time interval between 36 and 96 hours the values of the tortuosity firstly increase and then drop to values provided by Equations (24) where the damage variable D is close to one, see Figure 10(b). In this regard, is worth underlining that some of the curves perfectly overlap in the first part of the simulated time due to the time required for the accumulation of salt, stress, damage, etc.

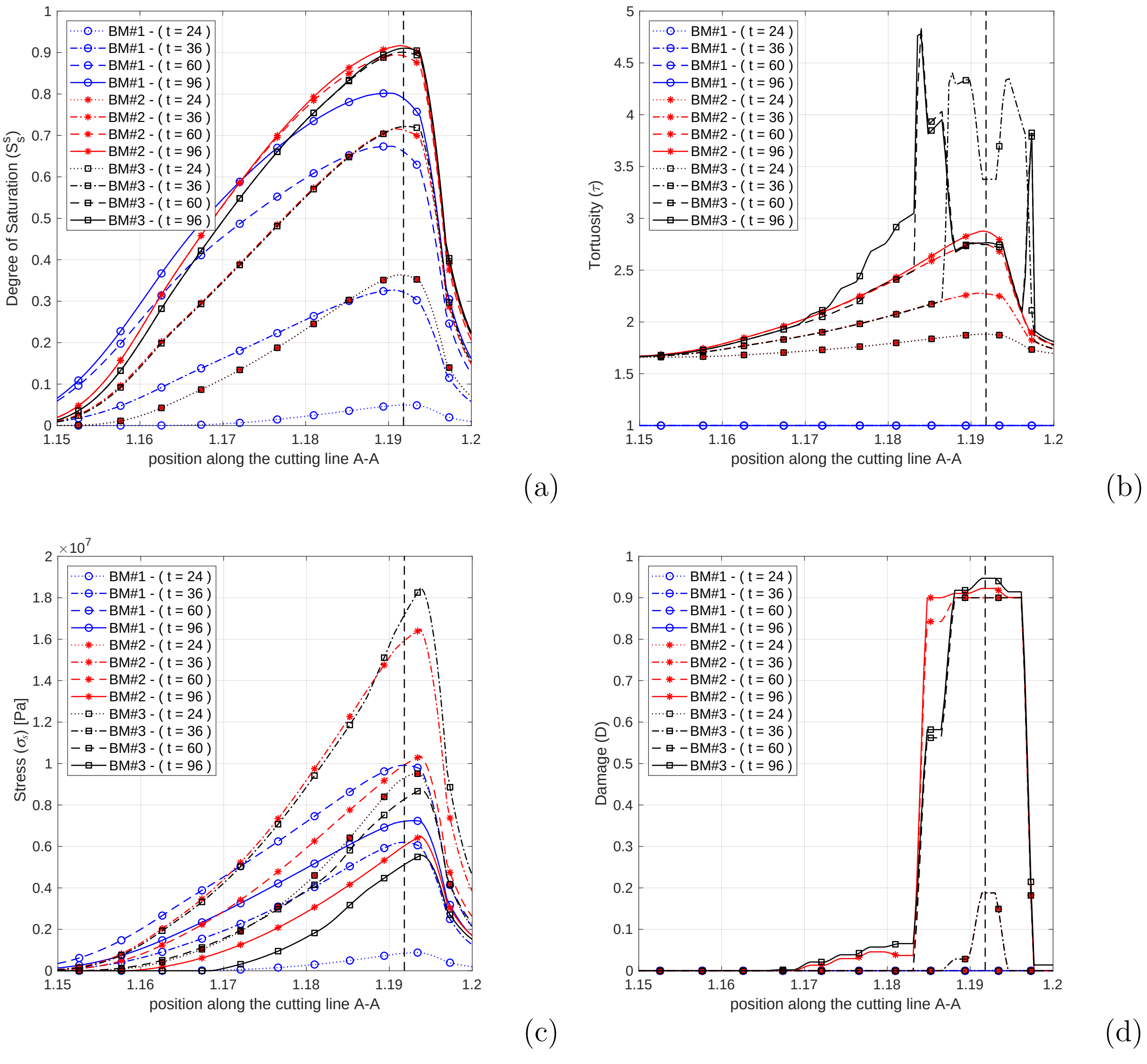

Figure 10: Benchmarks results comparison: illustration of fields variation for $t = [24, 36, 60, 96]$; degree of saturation S_s^s (a), the tortuosity τ (b), the stress σ_s (c) and damage variable D (d).

8. Conclusions

A staggered multiphysics framework for the numerical simulation of salt crystallization-induced damage in porous building materials, such as masonry, was presented and discussed. This framework is based upon a multiphase model to account for salt transport and crystallization within a porous the porous material and a mechanical model to account for the mechanical damage of the material. The solution algorithm is composed of a two-way data exchange between the multiphase and the mechanical models. Firstly, crystallization pressure information is passed to the mechanical model to analyze the mechanical response of the material. Secondly, the mechanical outcomes (e.g. damage distribution) are used to update some multiphase model properties (e.g. tortuosity) allowing simulations also beyond the onset of damage. Few simple geometry-based relationships are discussed to update multiphase model properties along with damage.

Numerical examples are used to show the capability of the proposed staggered framework for simulating complex interactions among salt transport, salt crystallization, and damaging within the porous material. Numerical results highlight the potential influence of updating multiphase model properties along with damage to conduct simulations also beyond the onset of damage. Further investigations could be also devoted to the role of the pore size since, in general, the maximum tortuosity does not correspond to the minimal porosity. Accordingly, the tortuosity would not only be a function of the porosity but also of the pore structure of the porous material.

Acknowledgement

The support from the European project CRYSTINART through the Joint Programming Initiative on Cultural Heritage (JPI-CH) is hereby acknowledged.

Appendix A. Sensitivity analyses

Appendix A.1. Mesh refinement

BM#3 is used with uniform mesh refinements in both directions ($N_x \times N_y$) using $N_x = [50, 100, 200]$ and $N_y = [1, 3, 5]$. Figures A.11, illustrates the results obtained for super-saturation ratio ω/ω_{sat}, the tortuosity τ, the stress distribution $\overline{\sigma}_s$ and damage variable D respectively, using $N_y = 1$ and $N_y = 3$. As expected, Figure A.11 shows a variation in time for variables depending on the mesh density close to the surface, i.e. where the stress variation is severe. Nevertheless, according to these results the solution obtained using $N_x = 100$ (independently from the value of Ny) are comparable. This aspect is mainly due to the specific definition of the EBC which defines a 1D-like problem.

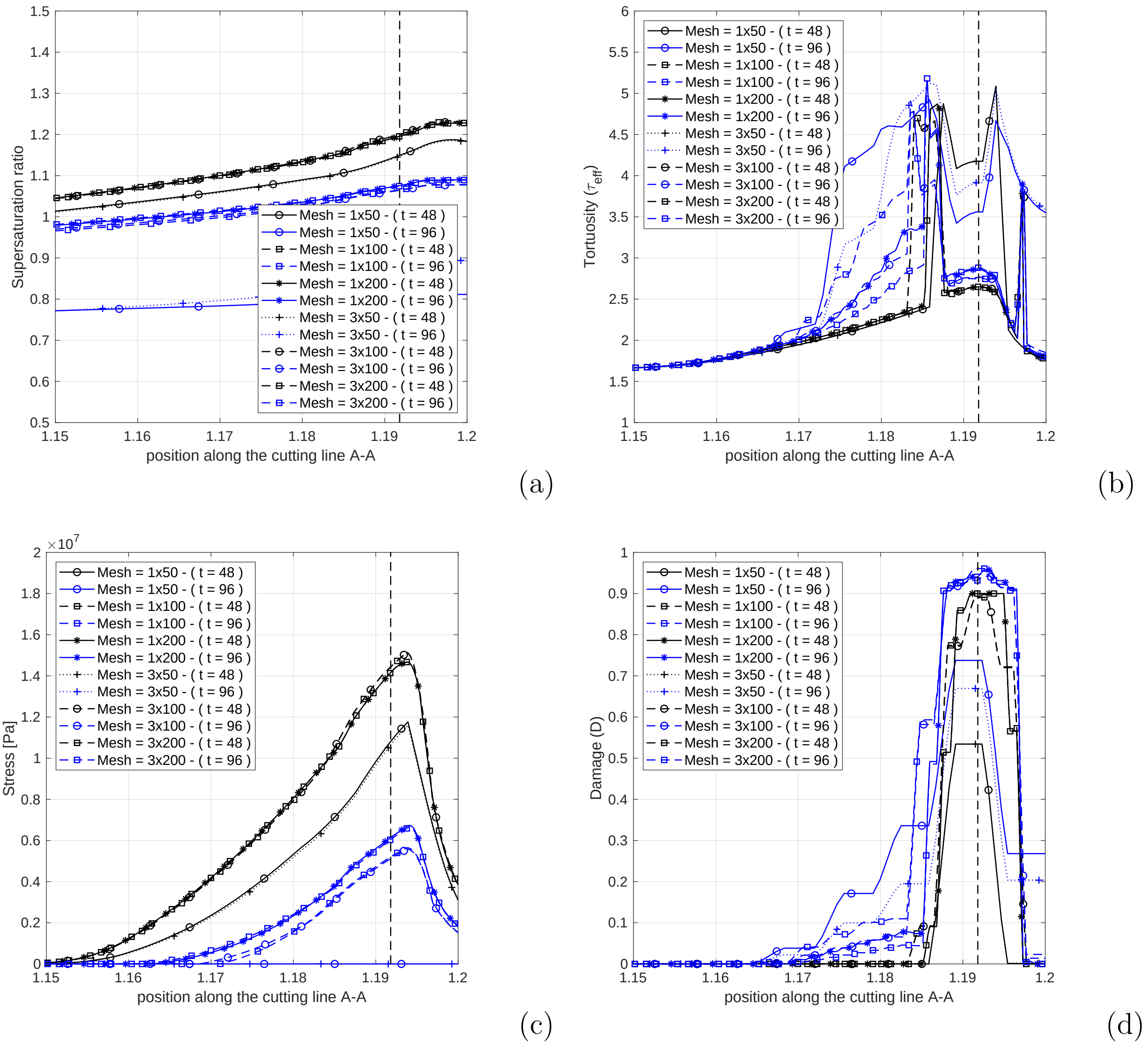

Figure A.11: Benchmark#3 - mesh sensitivity: Damage, Stress and Tortuosity - Mesh 1x50, 1x100, 1x200 and Mesh 3x50, 3x100, 3x200 - Time Slot $\Delta t = [48, 96]$ hours, $D^* = 0.2$

Appendix A.2. Time slot staggered sequence

The sensitivity of the FTO time interval is tested for several Δt values. Results are shown in terms tortuosity $\tau(\phi_{eff}, D, D^*)$, averaged stress $\overline{\sigma}_s$ and the single degradation damage variable D plots: along the cutting line $A - A'$ for $t = [48, 96]$ hours Figure A.12(a), and for different sampling at $x = 1.1918$ Figure A.12(b) for $\Delta t = [1, 2, 6, 12, 24]$ hours.
By inspecting Figure A.12, it is possible to note that the evolution of the averaged stress is slightly depending on the definition of the time interval Δt, on all the solutions are matching the reference solution obtained using $\Delta t = 1$.

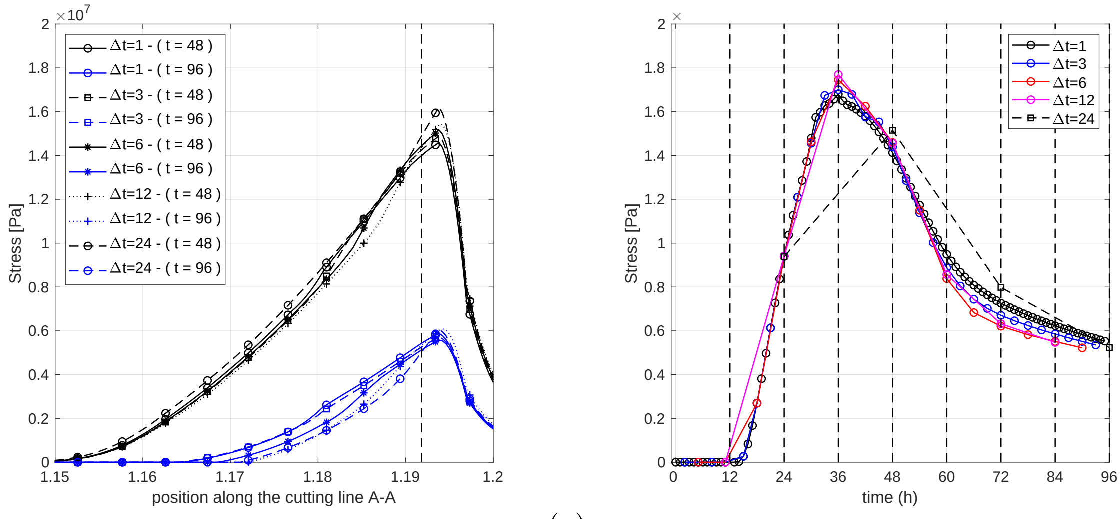

(a) (b)

Figure A.12: Staggered time intervals sensitivity - stress field evaluated using FTO time intervals equal to $\Delta t = [1, 3, 6, 12, 24]$ along the time evolution at $x = 1.1918$ (a) and along the $A - A'$ section for $t = [48, 72]$ hours (b).

The influence of the choice of time sampling on the effective tortuosity is shown in Figure A.13. By inspecting Figure A.13 it is possible to note that the evolution of the tortuosity is characterized by quick variation in time. Accordingly, tortuosity tends to rapidly increasing as soon as the single degradation damage variable is different from zero, but it also rapidly decreases when the single degradation damage variable reaches the damage threshold D^*, this rapid variation takes 6-8 hours in total when measured at point $x = 1.1918$, see Figure A.13(a) for $\Delta t = 1$ hours. Therefore, models that are transferring information between fields using $\Delta t \geq 6$ cannot record this rapid variation. As a matter of fact, solutions obtained with $\Delta t = [12, 24]$ are diverging from the reference solution ($\Delta t = 1$) whether solutions obtained with $\Delta t = [3, 6]$ are matching the reference solution. Similar evidence can be described for the resulting damage D in Figure A.14.

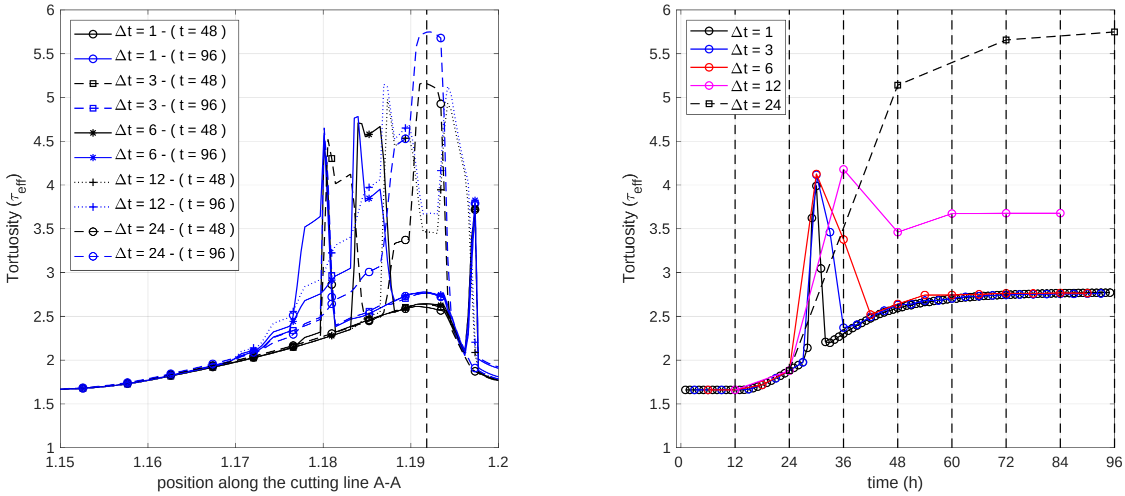

(a) (b)

Figure A.13: Staggered time intervals sensitivity - tortuosity field evaluated using FTO time intervals equal to $\Delta t = [1, 3, 6, 12, 24]$ along the time evolution at $x = 1.1918$ (a) and along the $A - A'$ section for $t = [48, 72]$ hours (b).

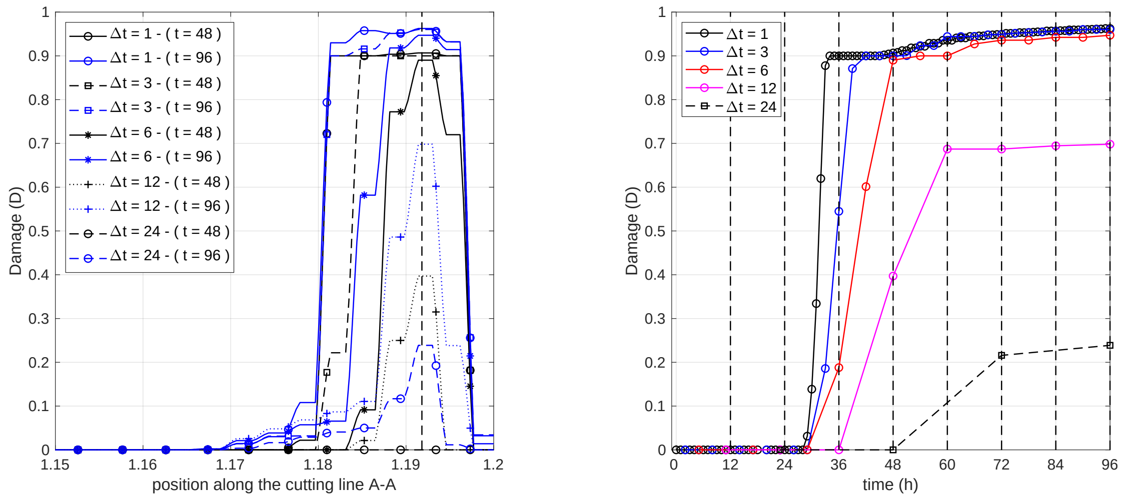

(a)

(b)

Figure A.14: Staggered time intervals sensitivity - damage field variable evaluated using FTO time intervals equal to $\Delta t = [1, 3, 6, 12, 24]$ along the time evolution at $x = 1.1918$ (a) and along the $A - A'$ section for $t = [48, 72]$ hours (b).

Appendix A.3. Kinetic law power law exponent

The power P appearing in the growth rate law in Equation (13), is the crystallization process order depending on the properties of the porous material and the salt present in the saline solution. We investigated five cases with the process order equal to: P = [0.5, 1.0, 2.0, 3.0, 5.0] for the BM#3 setup to test the robustness of the procedure, see Figure A.15 which refers to $t = 72$ hours. The parameter P depends on the salt type and influences the solution properties, crystal volume and crystallization pressure along with the shape and magnitude of the damaged area, see Figure A.15. As can be noted, the numerical approach appears robust and does not show stability problems by changing P.

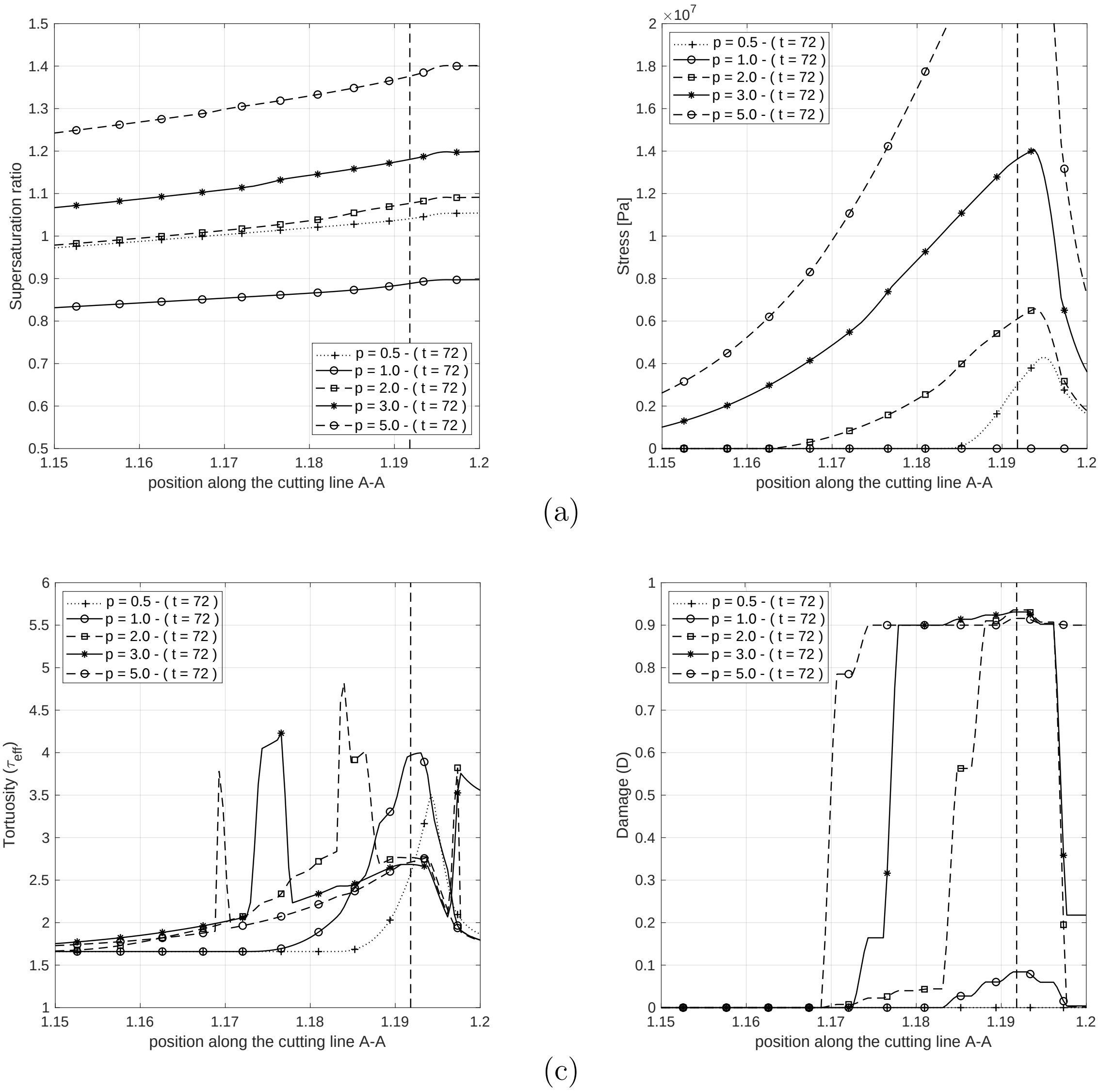

(a)

(b)

(c)

(d)

Figure A.15: Kinetic law power exponent: illustration of fields variation at $t = 72$ for $p = [0.5, 1.0, 2, 0, 3.0, 5.0]$: supersaturation ratio ω/ω_{sat} (a), the stress distribution $\overline{\sigma}_s$ (b), the tortuosity τ (c) and damage variable D (d) using a mesh formed by $N_x = 3$ and $N_y = 100$ elements and $\Delta t = 6$ hours.

References

[1] Alessandra Bonazza, Palmira Messina, Cristina Sabbioni, Carlota M Grossi, and Peter Brimblecombe. Mapping the impact of climate change on surface recession of carbonate buildings in europe. *Science of the total environment*, 407(6):2039–2050, 2009.

[2] Barbara Lubelli, Rob PJ van Hees, and Caspar JWP Groot. The role of sea salts in the occurrence of different damage mechanisms and decay patterns on brick masonry. *Construction and building materials*, 18(2):119–124, 2004.

[3] Robert J Flatt, Francesco Caruso, Asel Maria Aguilar Sanchez, and George W Scherer. Chemo-mechanics of salt damage in stone. *Nature communications*, 5(1):1–5, 2014.

[4] Noushine Shahidzadeh-Bonn, Julie Desarnaud, François Bertrand, Xavier Chateau, and Daniel Bonn. Damage in porous media due to salt crystallization. *Physical Review E*, 81(6):066110, 2010.

[5] Elisa Franzoni, Cristina Gentilini, Gabriela Graziani, and Simone Bandini. Towards the assessment of the shear behaviour of masonry in on-site conditions: A study on dry and salt/water conditioned brick masonry triplets. *Construction and Building Materials*, 65:405 – 416, 2014.

[6] Elisa Franzoni, Cristina Gentilini, Mattia Santandrea, and Christian Carloni. Effects of rising damp and salt crystallization cycles in frcm-masonry interfacial debonding: Towards an accelerated laboratory test method. *Construction and Building Materials*, 175:225 – 238, 2018.

[7] A.M. D'Altri and S. de Miranda. Environmentally-induced loss of performance in frp strengthening systems bonded to full-scale masonry structures. *Construction and Building Materials*, 249, 2020.

[8] S. Majid Hassanizadeh and Toon Leijnse. On the modeling of brine transport in porous media. *Water Resources Research*, 24(3):321–330, 1988.

[9] B Lubelli, RPJ Van Hees, and HJP Brocken. Experimental research on hygroscopic behaviour of porous specimens contaminated with salts. *Construction and Building Materials*, 18(5):339–348, 2004.

[10] Norman Epstein. On tortuosity and the tortuosity factor in flow and diffusion through porous media. *Chemical Engineering Science*, 44(3):777 – 779, 1989.

[11] Oliver Coussy. *Problems of Poroelasticity*, chapter 5, pages 113–150. John Wiley & Sons, Ltd, 2005.

[12] Carl W. Correns. Growth and dissolution of crystals under linear pressure. *Discuss. Faraday Soc.*, 5:267–271, 1949.

[13] Michael Steiger. Crystal growth in porous materials—i: The crystallization pressure of large crystals. *Journal of Crystal Growth*, 282(3):455 – 469, 2005.

[14] Rosa M Espinosa-Marzal and George W Scherer. Impact of in-pore salt crystallization on transport properties. *Environmental earth sciences*, 69(8):2657–2669, 2013.

[15] George W. Scherer. Stress from crystallization of salt. *Cement and Concrete Research*, 34(9):1613–1624, 9 2004.

[16] Julie Desarnaud, Daniel Bonn, and Noushine Shahidzadeh. The pressure induced by salt crystallization in confinement. *Scientific reports*, 6(1):1–8, 2016.

[17] Olivier Coussy. Deformation and stress from in-pore drying-induced crystallization of salt. *Journal of the Mechanics and Physics of Solids*, 54(8):1517–1547, 2006.

[18] Barbara Lubelli, Rob PJ van Hees, and Timo G Nijland. Salt crystallization damage: how realistic are existing ageing tests. In *Proceedings of the international conference on ageing of materials and structures, Delft*, pages 103–111, 2014.

[19] Marcin Koniorczyk and Dariusz Gawin. Modelling of salt crystallization in building materials with microstructure – poromechanical approach. *Construction and Building Materials*, 36:860 – 873, 2012.

[20] Marcin Koniorczyk, Dariusz Gawin, and Bernhard A Schrefler. Multiphysics model for spalling prediction of brick due to in-pore salt crystallization. *Computers & Structures*, 196:233–245, 2018.

[21] Hannelore Derluyn, Peter Moonen, and Jan Carmeliet. Deformation and damage due to drying-induced salt crystallization in porous limestone. *Journal of the Mechanics and Physics of Solids*, 63:242 – 255, 2014.

[22] G. Castellazzi, C. Colla, S. De Miranda, G. Formica, E. Gabrielli, L. Molari, and F. Ubertini. A coupled multiphase model for hygrothermal analysis of masonry structures and prediction of stress induced by salt crystallization. *Construction and Building Materials*, 41:717–731, 2013.

[23] G. Castellazzi, S. de Miranda, L. Grementieri, L. Molari, and F. Ubertini. Multiphase model for hygrothermal analysis of porous media with salt crystallization and hydration. *Materials and Structures/Materiaux et Constructions*, 49(3):1039–1063, 2016.

[24] L. Grementieri, L. Molari, H. Derluyn, J. Desarnaud, V. Cnudde, N. Shahidzadeh, and S. de Miranda. Numerical simulation of salt transport and crystallization in drying prague sandstone using an experimentally consistent multiphase model. *Building and Environment*, 123:289 – 298, 2017.

[25] L. Grementieri, F. Daghia, L. Molari, G. Castellazzi, H. Derluyn, V. Cnudde, and S. de Miranda. A multi-scale approach for the analysis of the mechanical effects of salt crystallisation in porous media. *International Journal of Solids and Structures*, 126-127:225–239, 2017.

[26] Jinhyun Choo and WaiChing Sun. Cracking and damage from crystallization in pores: Coupled chemo-hydro-mechanics and phase-field modeling. *Computer Methods in Applied Mechanics and Engineering*, 335:347 – 379, 2018.

[27] Jeeho Lee and Gregory L. Fenves. Plastic-damage model for cyclic loading of concrete structures. *Journal of Engineering Mechanics*, 124(8):892–900, 1998.

[28] Jihoon Kim, Eric Sonnenthal, and Jonny Rutqvist. A sequential implicit algorithm of chemo-thermo-poro-mechanics for fractured geothermal reservoirs. *Computers & Geosciences*, 76:59 – 71, 2015.

[29] William G. Gray and Cass T. Miller. Thermodynamically constrained averaging theory approach

for modeling flow and transport phenomena in porous medium systems: 1. motivation and overview. *Advances in Water Resources*, 28(2):161 – 180, 2005.

[30] Jan Sýkora, Tomáš Krejčí, Jaroslav Kruis, and Michal Šejnoha. Computational homogenization of non-stationary transport processes in masonry structures. *Journal of Computational and Applied Mathematics*, 236(18):4745 – 4755, 2012. FEMTEC 2011: 3rd International Conference on Computational Methods in Engineering and Science, May 9–13, 2011.

[31] Nicolai Andreas. Modeling and numerical simulation of salt transport and phase transitions in unsaturated porous building materials.

[32] G.E. Archie. The electrical resistivity log as an aid in determining some reservoir characteristics. *Transactions of the AIME*, 146:54–62, 1942.

[33] Jacques Comiti and Maurice Renaud. A new model for determining mean structure parameters of fixed beds from pressure drop measurements: application to beds packed with parallelepipedal particles. *Chemical Engineering Science*, 44(7):1539 – 1545, 1989.

[34] Harold L. Weissberg. Effective diffusion coefficient in porous media. *Journal of Applied Physics*, 34(9):2636–2639, 1963.

[35] E. Mauret and M. Renaud. Transport phenomena in multi-particle systems—i. limits of applicability of capillary model in high voidage beds-application to fixed beds of fibers and fluidized beds of spheres. *Chemical Engineering Science*, 52(11):1807 – 1817, 1997.

[36] M. Barrande, R. Bouchet, and R. Denoyel. Tortuosity of porous particles. *Analytical Chemistry*, 79(23):9115–9121, 2007.

[37] A. Koponen, M. Kataja, and J. Timonen. Tortuous flow in porous media. *Phys. Rev. E*, 54:406–410, Jul 1996.

[38] Nader Ghafoori and Shivaji Dutta. Laboratory investigation of compacted no-fines concrete for paving materials. *Journal of Materials in Civil Engineering*, 7(3):183–191, 1995.

[39] Joe D. Luck, Stephen Ray Workman, Stephen F. Higgins, and Mark S. Coyne. Hydrologic properties of pervious concrete. *Transactions of the ASABE*, 49:1807–1813, 2006.

[40] Maciej Matyka and Zbigniew Koza. How to calculate tortuosity easily? *AIP Conference Proceedings*, 1453(1):17–22, 2012.

[41] M. Karoglou, A. Moropoulou, Z.B. Maroulis, and M.K. Krokida. Water sorption isotherms of some building materials. *Drying Technology*, 23(1-2):289–303, 2005.

[42] Marcin Koniorczyk and Dariusz Gawin. Heat and moisture transport in porous building materials containing salt. *Journal of Building Physics*, 31(4):279–300, 2008.

[43] Lisa grementieri. Modelling and analysis of mechanical effect s induced by salt crystallisation in porous building materials: a two- scale approach.

[44] Michael Steiger, Jana Kiekbusch, and Andreas Nicolai. An improved model incorporating pitzer's equations for calculation of thermodynamic properties of pore solutions implemented into an efficient program code. *Construction and Building Materials*, 22(8):1841–1850, 2008.

[45] Michael Steiger. Crystal growth in porous materials—ii: Influence of crystal size on the crystallization pressure. *Journal of Crystal Growth*, 282(3):470 – 481, 2005.

[46] L. Dormieux, D. Kondo, and F.-J. Ulm. *Linear Microporoelasticity*, chapter 5, pages 137–165. John Wiley & Sons, Ltd, 2006.

[47] Bharath Vijayaraghavan, David R. Ely, Yet-Ming Chiang, Ramiro García-García, and R. Edwin García. An analytical method to determine tortuosity in rechargeable battery electrodes. *Journal of The Electrochemical Society*, 159(5):A548–A552, 2012.

[48] S. de Miranda, A.M. D'Altri, and G. Castellazzi. Modeling environmental ageing in masonry strengthened with composites. *Engineering Structures*, 201, 2019.

[49] COMSOL Multiphysics®. COMSOL AB, Stockholm, Sweden.

[50] B. Simon. Dissolution rates of nacl and kcl in aqueous solution. *Journal of Crystal Growth*, 52:789–794, 1981.

[51] Noushine Shahidzadeh-Bonn, Julie Desarnaud, Fran çois Bertrand, Xavier Chateau, and Daniel Bonn. Damage in porous media due to salt crystallization. *Phys. Rev. E*, 81:066110, Jun 2010.

[52] Rosa Maria Espinosa, Lutz Franke, and Gernod Deckelmann. Phase changes of salts in porous materials: Crystallization, hydration and deliquescence. *Construction and Building Materials*, 22(8):1758–1773, 2008.

[53] J. Ahl. Salt diffusion in brick structures part ii the effect of temperature, concentration and salt. *Journal of Materials Science*, 39(13):4247–4254, 2004. cited By 13.